JOURNAL OF SYNCHROTRON RADIATION
ISSN 1600-5775

High-pressure Seebeck coefficients and thermoelectric behaviors of Bi and PbTe measured using a Paris-Edinburgh cell

Jason Baker,[a] Ravhi Kumar,[a]* Changyong Park,[b]* Curtis Kenney-Benson,[b] Andrew Cornelius[a] and Nenad Velisavljevic[c]

[a]HiPSEC and Department of Physics, University of Nevada, Las Vegas, 4505 South Maryland Parkway, Las Vegas, NV 89154, USA, [b]HPCAT, Geophysical Laboratory, Carnegie Institution of Washington, 9700 South Cass Avenue, Argonne, IL 60439, USA, and [c]Shock and Detonation Physics Group, Los Alamos National Laboratory, Los Alamos, NM 87545, USA. *Correspondence e-mail: ravhi@physics.unlv.edu, cpark@carnegiescience.edu

Received 13 April 2016
Accepted 13 September 2016

Edited by Y. Amemiya, University of Tokyo, Japan

Keywords: thermoelectrics; Paris-Edinburgh press; Seebeck coefficient; thermal conductivity; high pressure.

A new sample cell assembly design for the Paris-Edinburgh type large-volume press for simultaneous measurements of X-ray diffraction, electrical resistance, Seebeck coefficient and relative changes in the thermal conductance at high pressures has been developed. The feasibility of performing *in situ* measurements of the Seebeck coefficient and thermal measurements is demonstrated by observing well known solid–solid phase transitions of bismuth (Bi) up to 3 GPa and 450 K. A reversible polarity flip has been observed in the Seebeck coefficient across the Bi-I to Bi-II phase boundary. Also, successful Seebeck coefficient measurements have been performed for the classical high-temperature thermoelectric material PbTe under high pressure and temperature conditions. In addition, the relative change in the thermal conductivity was measured and a relative change in ZT, the dimensionless figure of merit, is described. This new capability enables pressure-induced structural changes to be directly correlated to electrical and thermal properties.

1. Introduction

Thermoelectric materials have a vast array of applications from commercial thermoelectric refrigeration to energy-efficient engines in the automotive industry. However, their effectiveness, as expressed in the dimensionless figure of merit given by $ZT = (\alpha^2\sigma/\kappa)T$, where α is the Seebeck coefficient, σ is the electrical conductivity, κ is the thermal conductivity and T is the temperature, has certain limitations (DiSalvo, 1999; Chung *et al.*, 2000; Sales, 2002). Improving thermoelectric materials requires an ever advancing efficiency. Pressure tuning has the potential to provide insight into the effect of structure and volume change on the figure of merit, which can be used for reverse engineering development of new and improved thermoelectric materials (Badding *et al.*, 1998). In order to characterize and better understand these materials, the physical properties related to thermoelectric efficiency must be studied in detail. Electrical resistivity, Seebeck coefficient and thermal conductivity are important variables connected to the thermoelectric efficiency (DiSalvo, 1999), and high-pressure experiments measuring the thermal and electrical properties both individually and simultaneously are imperative due to the interplay of these properties.

X-ray diffraction (XRD) measurements have been and continue to be the most widely used technique for studying

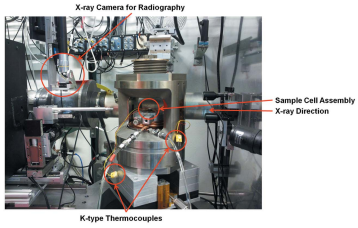

material properties under high pressure–temperature (P–T) conditions. Based on XRD measurements one can directly determine P–V–T conditions as well as detect the structural phase transitions as a function of P–T. Although XRD techniques provide valuable information about structural phase transformations and even detection of solid-melt transition, detection of many associated property changes, such as variation in thermal and electrical conductivity, change in magnetic ordering, *etc*., requires development of new experimental probes. One example where such measurements are crucial is the study of thermoelectric materials. To truly understand any changes in physical properties at high pressures it is imperative to correlate the properties to volume and/or structural changes.

P. W. Bridgman was first to introduce electrical resistance measurements in high P–T experiments with opposed anvil type pressure apparatus (Bridgman, 1952). Bridgman also made the first attempts at measuring thermal properties of materials under high-pressure conditions (Bridgman, 1922). Errandonea *et al.*, in addition to others, have utilized this opposed anvil design developed by Bridgman to understand the behavior of transport properties at high pressure such as the Hall effect, electrical resistivity and thermopower measurements performed on CdTe, InSe, GaSe and ZnTe samples in addition to others (Errandonea *et al.*, 1997, 2005, 2009). However, these opposed anvil designs are not easily compatible with X-ray diffraction techniques, and simultaneous XRD and transport property measurements could not be performed. With the development of diamond anvil cells (DACs) and evolution of X-ray sources, the methods applied by Bridgman were further improved. Both higher pressure ranges and simultaneous structural, thermal and electrical measurements were developed and a large variety of experiments have been performed. Shchennikov *et al.* and Ovsyannikov *et al.* performed high-pressure electrical resistivity and thermopower measurements on PbTe, PbSe and ZnTe, and Fe_3O_4 single crystals (Shchennikov *et al.*, 2008; Ovsyannikov *et al.*, 2008*a*,*b*; Ovsyannikov & Shchennikov, 2004*a*,*b*). Ke *et al.* explored the electrical transport properties of SnS using specialized microcircuits on the surface of their DACs (Ke *et al.*, 2013). However, the drawbacks of using DACs are the very small sample volume (of the order of 10^{-4} mm^3) and difficulties in maintaining a substantial thermal gradient across the anvils during thermal property measurements. Alternatively, large-volume presses allow for use of larger sample volumes for both electrical resistance and thermal transport experiments. Recently, initial attempts at simultaneous measurement of the thermal diffusivity/conductivity and the Seebeck coefficient were made by Jacobsen *et al.* (2012) and Yuan *et al.* (2014) using large-volume multi-anvil press apparatus, with sample volume of the order of mm^3. With larger sample volume and evolution of multi-anvil apparatus, other experimental probes have also been introduced, such as ultrasonic interferometric sound velocity and electrical conductivity measurements (Yuan *et al.*, 2014; Li *et al.*, 1996, 2004; Li & Liebermann, 2007). In addition to the greatly increased sample volume, the easily recoverable samples also allow for continued analysis after the compression experiments.

While the aforementioned multi-anvil experiments demonstrate the ability to measure electrical and thermal properties, as well as the speed of sound, in materials at high P–T, these measurements did not provide a direct measurement of the sample dimensions. A significant step forward in high P–T studies is to couple XRD, thermal conductivity and electrical resistivity measurements along with *in situ* measurements of sample dimensions; this is obviously important as the sample dimensions will change during compression or heating in the large-volume press. By having the ability to monitor the sample behavior *in situ* through X-ray radiography, the dimensions of the sample can be measured under both ambient and high P–T conditions (Kono *et al.*, 2014). In our experiments with the large-volume Paris-Edinburgh (PE) type cell, we performed real-time monitoring of sample dimensions at high P–T using X-ray radiography.

Originally, the PE-type large-volume press was developed for use in neutron experiments (Klotz *et al.*, 2004). The cell assembly associated with the PE cell has been adapted for use in X-ray scattering experiments such as exploring high P–T phases of materials, ultrasonic measurements, viscosity measurements and high P–T synthesis of materials (Kono *et al.*, 2012, 2014; Morard *et al.*, 2007; Nieto-Sanz *et al.*, 2004). Also, recently, developments have been made in measuring electrical resistance with the PE cell as described by Matityahu *et al.* (2015).

In this article we describe the design and subsequent application of a dedicated sample cell assembly for the PE cell to perform measurements of the Seebeck coefficient and a relative change in the thermal conductivity under high P–T conditions, which can then be utilized to determine relative changes in ZT of materials. The addition of the ability to measure relative changes in the thermal conductivity and dimensionless figure of merit makes this technique unique among other experimental set-ups (Matityahu *et al.*, 2015; Yuan *et al.*, 2014; Li & Liebermann, 2007; Li *et al.*, 1996, 2004; Jacobsen *et al.*, 2012). Additionally, the apparatus is capable of performing simultaneous X-ray radiography imaging and X-ray diffraction with synchrotron radiation. Furthermore, the sample and experimental setup for this type of measurement is not necessarily constrained for use with a specific type of PE press but rather can be extended to other PE cell designs. The purpose of the developed cell assembly is to enable these individual measurements to be performed simultaneously. Measuring these properties simultaneously minimizes possible error in sample geometry and deterioration over time. The measurement capability with this assembly provides a valuable method of mapping the transport properties of a wide variety of materials under high P–T conditions and allows new opportunities for *in situ* studies of structure and property correlations, especially thermoelectric properties. In addition, this technique could also be used for other functional materials and actinide alloys.

2. Experimental methods

2.1. Cell assembly design

Shown in Fig. 1(*a*) is the experimental setup with a PE press at the 16-BM-B beamline at the Advanced Photon Source (APS). A pair of tungsten slits collimates incident white X-ray beam from the synchrotron source. The resulting X-ray diffraction signal from the sample is collected by a Ge solid-state detector (Ge-SSD). A large Huber stage holds the Ge-SSD allowing precise control of the 2θ angle in an energy-dispersive X-ray diffraction configuration. Detector channel-energy calibration is performed using NIST Co^{57} and Cd^{109} radioactive sources, while the detector 2θ position is calibrated using ambient P–T condition unit-cell parameters of MgO (Yamada *et al.*, 2011; Kono *et al.*, 2010).

The sample cell assembly developed for these high-pressure/high-temperature electrical and thermal measurements is a modified version of the cell assembly design from previously reported high-pressure melt structure measurements (Morard *et al.*, 2007). The capability of the newly designed cell for measuring electrical resistance and some basic thermal properties have been described previously (Baker *et al.*, 2014).

Fig. 1(*b*) depicts a schematic of the modified sample cell assembly specifically designed for measurement of electrical resistance, Seebeck coefficient and thermal gradient measurements. At the top and bottom of the cell assembly zirconia (ZrO_2) caps were positioned with a surrounding boron epoxy (BE) gasket. The BE gasket is 3 mm thick and has an outer diameter of 14 mm and an inner diameter of 6 mm. Within the BE gasket, an MgO ring with a 6 mm outer diameter and 2 mm inner diameter is situated. These materials provide good thermal insulation as well as support to the central column, allowing directed heat flow from the graphite heater to the sample and finally to the heat sink as indicated by the arrows in Fig. 1(*b*).

Through the central column, a temperature gradient is generated by an asymmetrically located thin (∼150 µm) graphite disc heater with a diameter of 5.5 mm. Two pieces of 50 µm-thick molybdenum foil, located at the top and bottom of the cell assembly, establish contact with the graphite heater and the tungsten carbide anvils. These molybdenum foils are not shown in the schematic of Fig. 1(*b*) but are clearly visible and labeled in Fig. 1(*c*), which is a radiography image of the cell assembly. The process of obtaining the radiography image and the ability to use it to determine thickness was described in detail previously by Kono *et al.* (2014). Voltage is applied between the two tungsten carbide anvils, causing current to flow into one molybdenum foil electrode, through the graphite heater, and out of the other Mo foil.

A ∼200 µm-thick MgO disc with diameter 6 mm and a 150 µm-thick mica disc with the same diameter are positioned directly above the graphite disc to provide thermal insulation between the heater and top anvil. Directly below the heater, enclosed by the MgO ring, a 500 µm-thick and 2 mm-diameter single-crystal diamond disc (Almax) is utilized to electrically isolate the sample from the heater while allowing maximal heat flow. The single-crystal diamond disc was intact and no significant cracking was observed up to 5.5 GPa. In addition, another diamond disc and an aluminium plug are situated directly beneath the sample, which act as a heat sink by connecting to the bottom tungsten carbide anvil. Even though modeling may be needed to provide a detailed heat flow map, in general the flow of heat is assumed to be along the sample column, as depicted by the arrows in (Fig. 1*b*), because of the large thermal conductivity of diamond. The aluminium plug also has a secondary purpose of providing a spacer to properly

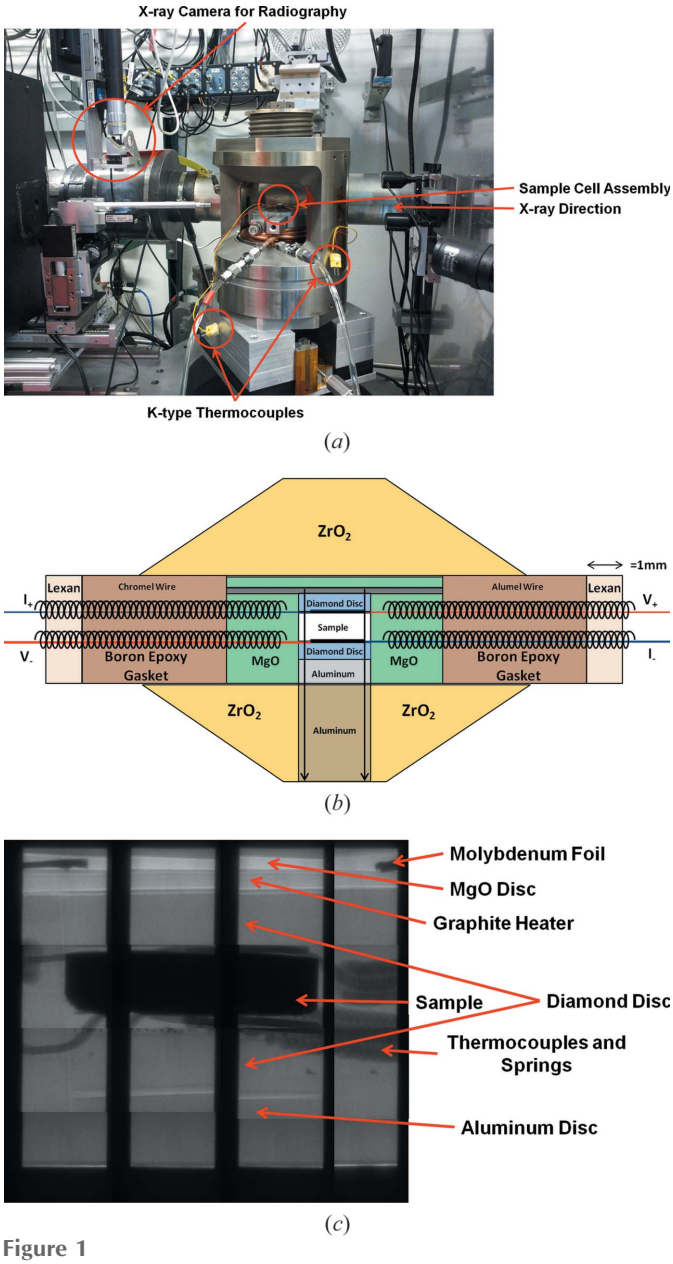

Figure 1
(*a*) Paris-Edinburgh set-up at HPCAT 16-BM-B beamline at the Advanced Photon Source, Argonne National Laboratory, with the sample cell assembly in place. (*b*) A scaled schematic design of the sample cell assembly. The top disc (colored green) represents an MgO and mica disc and the (gray) disc below represents the graphite heater. The two arrows represent the direction of heat flow. Also shown are the spring coils (not to size) that are explained in detail in the text. (*c*) Radiographic image of the sample cell assembly with labeled components.

position the sample in the center of the BE gasket and to obtain X-ray radiography imaging as shown in Fig. 1(*c*).

Two thermocouples are placed between the sample and the top and bottom diamond discs which act as thermal and electrical probes. The use of these thermocouples to measure electrical resistance in the cell assembly is described elsewhere (Baker *et al.*, 2014). K-type thermocouples were purchased from Omega Engineering as pre-made junctions of bare alumel and chromel wires with 125 µm diameter. The pre-made thermocouple junctions are then compressed between two flat tungsten carbide surfaces using a hand press to make a leaf-shaped thermocouple junction. This process reduces the thickness of the junction from 125 µm to about 70 µm. The thermocouples are then inserted into 600 µm holes drilled into the BE gasket. In order to minimize the potential of any shearing and breaking of the thermocouple wires during compression, each alumel and chromel wire is protected by covering with 'spring coils' made of the same material as the 125 µm-diameter wire. These spring coils slide over the respective alumel or chromel wire after the thermocouples have been inserted into the 600 µm holes and fill the space in the holes as shown in the schematic of Fig. 1(*b*).

2.2. Measurement of Seebeck coefficient

The Seebeck coefficient can be defined as the ratio of the thermoelectric voltage to the temperature difference across a material as given by equation (1),

$$\alpha_S = \Delta V/\Delta T, \tag{1}$$

where ΔV is the thermoelectric voltage as measured from the hot side to the cold side and ΔT is the temperature difference. A simple method is described by Polvani *et al.* (1999) to determine the Seebeck coefficient using thermocouples with known Seebeck coefficient as electrical leads independent of the environmental temperature. In our setup, the thermoelectric voltage is measured from the top thermocouple to the bottom thermocouple. Specifically, our experimental set-up uses K-type thermocouples with chromel and alumel wires as previously mentioned. The pressure effect on K-type thermocouples has been reported by Bundy (1961) to be at most 2°C per 100° ΔT over the pressure range 0–6 GPa. Additionally, more recent work performed by Nishihara *et al.* (2016) reports maximal changes in the Seebeck coefficient of alumel and chromel single wires as 2.5 µV K^{-1} at 900°C and 2 GPa. Nishihara *et al.* (2016) also report a temperature correction between 0 and 3°C throughout the entire pressure range 0–8 GPa. As such, within the typical error of K-type thermocouples, which is of the order of approximately 2°C, the pressure effect is negligible.

Equation (2) describes the Seebeck coefficient of the sample independent of ΔT, solely relying on the voltage measurements,

$$\alpha_S = \frac{\alpha_A - r\alpha_C}{1 - r}, \tag{2}$$

where r is the ratio of the alumel–alumel and chromel–chromel voltage differences ($r = \Delta V_{AA}/\Delta V_{CC}$), and α_A = −18.3 µV K^{-1} and α_C = 22.2 µV K^{-1} are the Seebeck coefficients of alumel and chromel, respectively. Fig. 2 shows a schematic view of the cell assembly depicting the voltage measurement in our experiment.

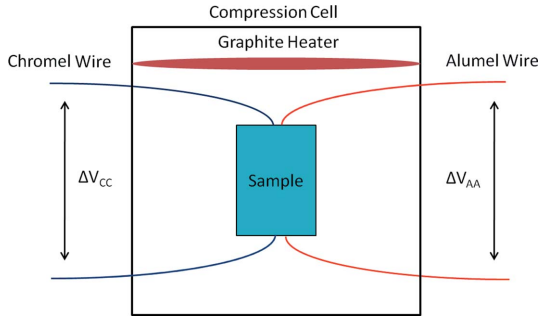

Figure 2
Schematic diagram depicting the voltages measured to determine the Seebeck coefficient of the sample. ΔV_{CC} is the voltage from the top to the bottom thermocouple chromel wires and ΔV_{AA} is the similar voltage for the alumel wires.

As a test sample, high-purity (99.99%) Bi powder purchased from Sigma-Aldrich was pressed into 2 mm-diameter and 500 µm-thick pellets using a tungsten carbide pellet die (from Hamasho Corporation). Several structural phases of bismuth are available within the pressure and temperature range provided by the PEC setup. A phase diagram of bismuth reported by Chen *et al.* (1997) is shown in Fig. 3(*a*) as reference. Experiments were performed over a wide range of temperature and pressure conditions to ensure consistency, reliability and to identify the ideal working conditions for our apparatus. In Fig. 3(*a*), arrows are shown to indicate the pathways taken in each experiment. Isobars were recorded at varying pressures to determine the Seebeck coefficient as a function of temperature, and an isothermal measurement was also performed over the pressure range 1–3.1 GPa to determine the pressure dependence of the Seebeck coefficient.

The PbTe system was chosen as a prime candidate for further study to test the capabilities of our system. PbTe has shown significant promise for increased thermoelectric efficiency in thermoelectric materials (Ovsyannikov & Shchennikov, 2007), and, as such, we wanted to explore the properties of this material using our apparatus. A small piece of an ingot of PbTe was ground finely into a powder using an agate mortar and pestle. After grinding the ingot of PbTe, the powder was put into the same 2 mm pellet die as used for the Bi experiments and a 2 mm-diameter and approximately 500 µm-thick pellet of PbTe was produced to be used as the sample. The Seebeck coefficient of PbTe was explored over the range shown in Fig. 3(*b*) where arrows indicate the temperature and pressure pathways taken in the measurements.

In Fig. 4(*a*) a plot of the voltage as a function of temperature for the Bi sample is displayed at 1.1 GPa, corresponding to path C in Fig. 3(*a*). In Fig. 4(*b*) a plot of the voltage as a function of temperature is shown for PbTe corresponding to path F in Fig. 3(*b*). The voltage values measured throughout these experiments have minimum values typically in the µV

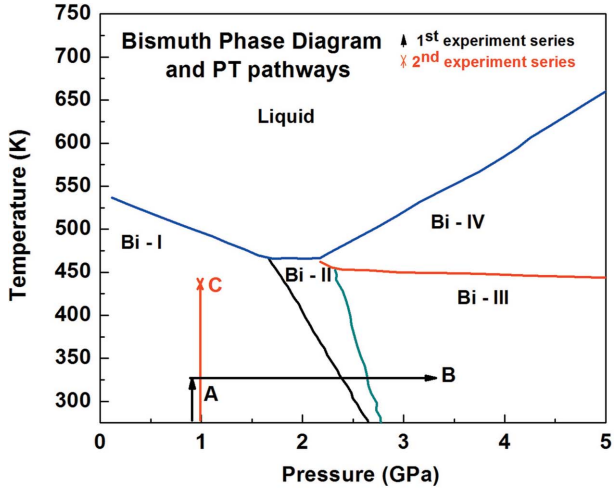

(*a*)

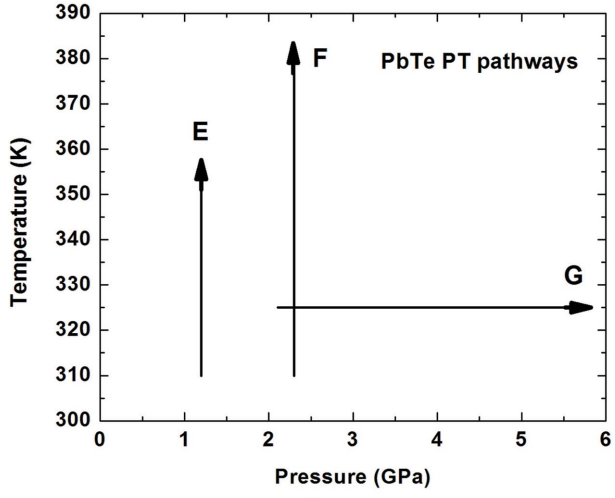

(*b*)

Figure 3
(*a*) Phase diagram of bismuth (Chen *et al.*, 1997). The arrows indicate the paths taken for each experiment series to determine the Seebeck coefficient. The paths are labeled corresponding to the experiment series. (*b*) Temperature and pressure pathways taken for the PbTe measurements to determine the Seebeck coefficient. PbTe remains in a single phase over the tested PT range.

range and a maximum in the mV range. The Agilent U3606B multimeter DC power supply was kept in the highest resolution range throughout the course of these experiments and, as such, the typical error on all voltages measured was ± 8 µV, which is smaller than the size of the symbol. By applying error propagation to equation (2) and using the errors determined from the Agilent U3606B voltage measurements, the error on our Seebeck coefficient measurements was determined and is included in the results.

Fig. 4(*a*) depicts the voltages as measured for Bi in a region devoid of a phase boundary and, as such, the voltage remains largely linear over the entire temperature range. Fig. 4(*b*) displays the voltages measured for the PbTe sample in a region devoid of a phase transition. The slight curvature at temperatures below 315 K is likely to be due to the small temperature difference across the sample creating very small voltages. After 315 K, the voltages follow a linear trend similar

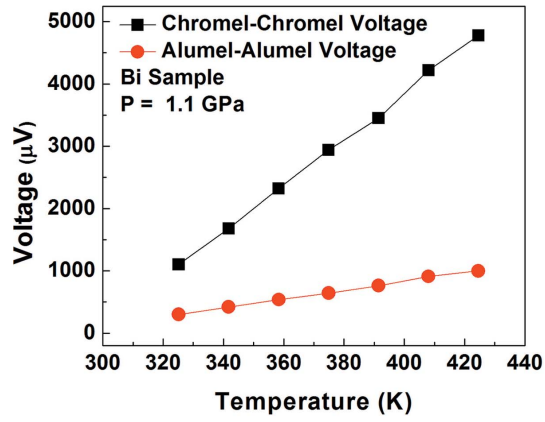

(*a*)

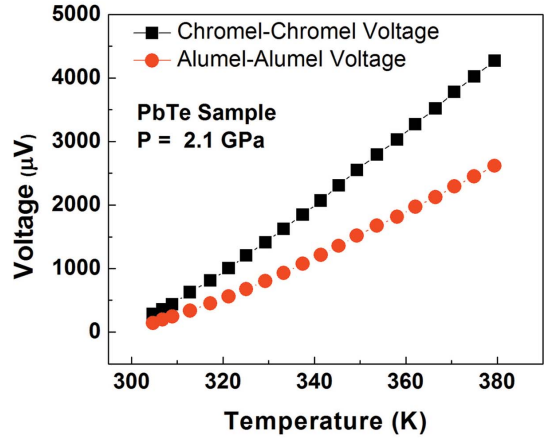

(*b*)

Figure 4
(*a*) Voltages (ΔV_{AA} and ΔV_{CC}) as measured with increasing temperature for the Bi sample at 1.1 GPa. The monotonous variation implies the absence of a structural phase transition at these temperatures and pressure. (*b*) Voltages (ΔV_{AA} and ΔV_{CC}) as a function of temperature for the PbTe sample at 2.1 GPa.

to the Bi measurements. With these voltage measurements, the Seebeck coefficient can be calculated using equation (2).

Small deviations in the pressure were measured as temperature was increased using the MgO ring as a pressure marker. Typically the pressure decreased slightly (0.1–0.2 GPa) as measured directly from the MgO. As the isobars were measured near 1 GPa and 2 GPa, these deviations are small compared with the changes observed in the voltage and Seebeck coefficient measurements.

2.3. Relative thermal conductance measurements

The thermal conductivity can be determined from

$$\kappa = \frac{P\Delta X}{A\Delta T}, \tag{3}$$

where P is the heater power received, ΔX is the thickness of the sample, A is the cross-sectional area of the sample and ΔT is the change in temperature across the sample. The temperature difference is measured using the K-type thermocouples as mentioned previously, and the cross-sectional area is determined by the diameter of the sample (2 mm). The heater power received by the sample is given by the simple

relation $P = IV$ in the ideal case, where V is the voltage applied to the graphite heater and I is the current through the heater.

For our experiments, the power is set to a particular value and a PID feedback loop controls the voltage and current to give a constant power input to the graphite heater. However, due to heat loss through the surrounding cell parts, the absolute power to the sample is unknown. Without knowing the absolute power, the thermal conductivity cannot be determined accurately. However, if the power loss remains constant with pressure per given cell configuration, a relative change in the thermal conductance can be extracted and utilized to determine the relative variation in the figure of merit for the samples. Typically, at least 5–10 min is given for the cell assembly to reach thermal equilibrium after increasing the power input. If the time is increased further than 10 min, the effect on the final temperature is small.

The thickness of the sample is monitored throughout the experiment, but specifically it is measured directly at each new pressure. As previously mentioned, and as shown in Fig. 1(*c*), X-ray radiographic imaging is used to view the cell assembly at both elevated temperatures and high pressures. By calibrating a length scale for the images of 0.95 µm pixel^{-1}, the thickness can be obtained by plotting the absorption as a function of pixels and determining the number of pixels between the edges of the sample. Fig. 5(*a*) shows a sample radiography image of the center of the sample and the red arrow indicates the position where the thickness is measured. Fig. 5(*b*) shows the absorption plot for this sample radiography image, and the thickness is determined by using the pixel location of the half-maximum of each edge. Fig. 6 shows the variation of sample thickness with pressure for Bi and PbTe. With all of these parameters determined, the thermal conductivity can be calculated. Due to the unknown heat losses, only the relative change in the thermal conductivity will be discussed and normalized to the largest value.

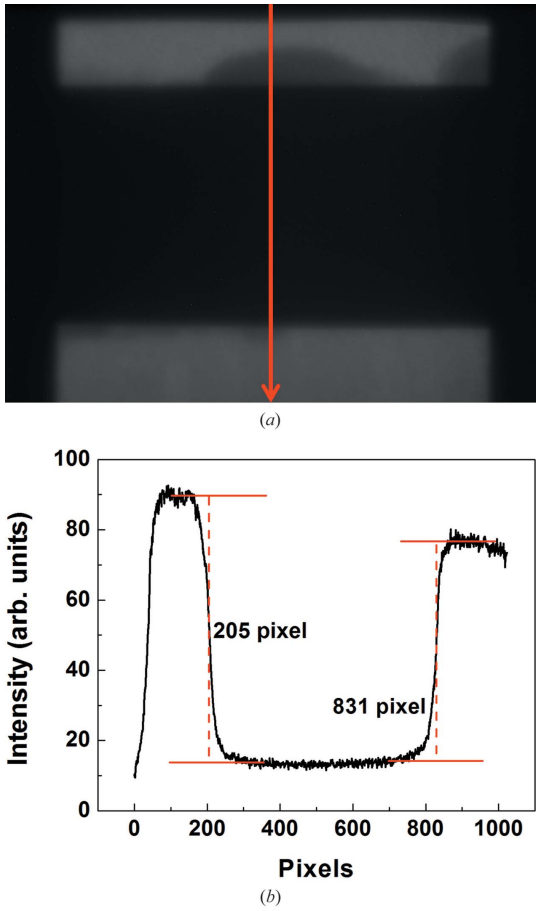

Figure 5
(*a*) Radiographic image of the center of the sample. The arrow corresponds to the particular path used to determine sample thickness. (*b*) Pixel intensity is plotted as a function of the pixel location to determine the thickness of the sample. The solid lines indicate the maximum and minimum of the edge and the dotted line is provided as a guide to help find the center, which is given for each edge.

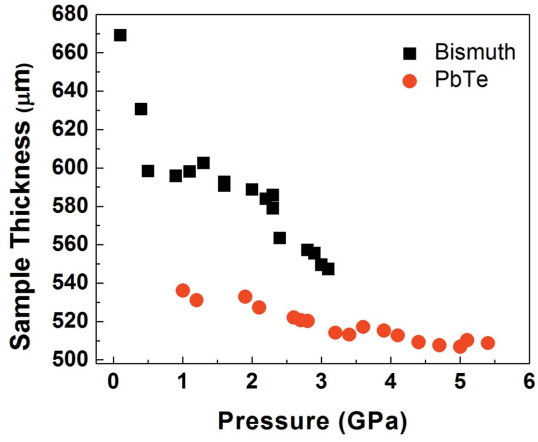

Figure 6
Plot of the sample thickness variation with compression for both the Bi and PbTe sample. The Bi sample initially was a thicker sample than the PbTe.

3. Results and discussion

3.1. Isobaric Seebeck coefficient of Bi

Fig. 7 shows the results of the isobaric measurements of the Seebeck coefficient performed on the Bi sample. Figs. 7(*a*) and 7(*b*) represent the plots of the Seebeck coefficient as a function of temperature corresponding to the paths labeled A and C, respectively, in Fig. 3(*a*). We have collected isobars, the first at 0.8 GPa and the second at 1.1 GPa, which both lie in a region with no known phase transition in order to understand the behavior of the Seebeck coefficient under these conditions. Also, Figs. 7(*a*) and 7(*b*) show no significant change in the Seebeck coefficient over the temperature range studied at these pressures. Fig. 7(*a*) has a small temperature range of only 305 K to 325 K and over this temperature window there is almost no change in the Seebeck coefficient as portrayed in the plot. The temperature for this experiment was kept low because an isotherm was taken at 325 K to obtain the Seebeck coefficient as a function of pressure for Bi. Fig. 7(*b*) has a temperature range of 325 K to 425 K which was chosen to give a large enough temperature range to see changes in the Seebeck coefficient and was kept low enough to ensure that

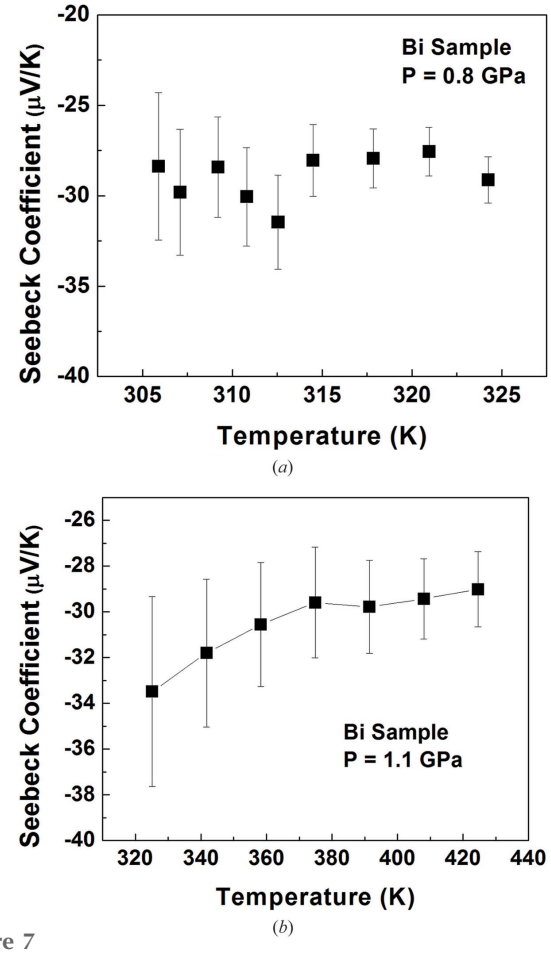

Figure 7
Isobaric Seebeck coefficient measurements for Bi at (*a*) 0.8 GPa and (*b*) 1.1 GPa from separate experimental runs.

the experiment stayed well below the liquid phase which occurs near 500 K at this pressure as shown in Fig. 3(*a*) (Chen *et al.*, 1997). Over the temperature range of 320 K to 360 K a slight variation in the average value of the Seebeck coefficient is observed, and upon further increasing the temperature the Seebeck coefficient stays constant. Due to the large size of standard errors, however, the variations look insignificant.

On comparing the Seebeck coefficient in our measurements at 0.8 GPa and 1.1 GPa near 300 K with the measurements performed by Ferdin *et al.* (1995), we found a difference in absolute values. Our measurements give a value of approximately -34 ± 4 μV K^{-1} at 1.1 GPa and 325 K and Ferdin *et al.* (1995) measurements yield approximately -60 μV K^{-1}. This difference may be contributed to by the sensitivity of the electronic properties of Bi to small impurities and the different sample forms with pelleted powder and single crystal, respectively. Chandrasekhar (1959) performed Seebeck measurements on single-crystal Bi samples and concluded a significant difference in the Seebeck coefficient caused by changing the orientation of the threefold symmetry of the Bi crystal. The polycrystalline nature of our samples alleviates the significance of orientation; however, if any preferred orientation is introduced when pressurizing the sample, it may contribute to the variations. Although there is a significant difference in the values between our measurements and those of Ferdin *et al.* (1995), the values shown in Figs. 7(*a*) and 7(*b*) are from separate experimental runs and thus provide evidence for consistency for our apparatus when measuring the Seebeck coefficient under the given experimental conditions.

3.2. Isothermal Seebeck coefficient, thermal conductivity and figure of merit for Bi

Fig. 8(*a*) displays the results of isothermal Seebeck coefficient measurements on the Bi sample over the pressure range 1.1–3.1 GPa both for compression and decompression cycles. These measurements correspond to the path labeled B in Fig. 3(*a*) that crosses the Bi-I to Bi-II phase boundary approximately at 2.5 GPa. The significant change and polarity change in the Seebeck coefficient from a value of -24 ± 2 μV K^{-1} to a value of $+19.3 \pm 0.3$ μV K^{-1} with increasing pressure from 2 GPa to 2.7 GPa coincides well with the phase boundary. The same trend is also observed in the decreasing pressure data shown in Fig. 8(*a*); however, there is a significant hysteresis within the Bi-I phase during the decompression cycle. The observed hysteresis could be due to unreported cell dynamics upon decompressing, but, as the polarity cross-over reproduces the consistent phase boundary around 2.5 GPa, we do not rule out the possibility that the result may indicate an intrinsic thermoelectric hysteresis with pressure, which requires further studies to fully understand. Upon complete decompression, the Seebeck coefficient recovers its initial value observed prior to the Bi-I to Bi-II phase transition.

Measurements performed by Ferdin *et al.* (1995) show a similar trend for the Seebeck coefficient as a function of pressure. Although the trend agrees, there is a difference between the values as measured in our experiment when compared with those reported by Ferdin *et al.* (1995). As discussed for the results of the temperature measurements, the differences between the two measurements may be attributed to different experimental conditions.

Fig. 8(*b*) plots the relative change in the thermal conductance as the sample is compressed. Although there is some scatter in the measured data below 2.3 GPa, it seems to follow a linear, generally increasing, trend as pressure is increased. The relative thermal conductance is observed to reach a maximum at approximately 2.3 GPa, and then it slowly decreases from the maximum value. This maximum in the relative thermal conductance corresponds reasonably well with the beginning of the phase transition and the onset of the change observed in the Seebeck coefficient measurement as shown in Fig. 8(*b*). Also, the slower decrease observed after 2.5 GPa corresponds with the Bi-I to Bi-II to Bi-III phase transition boundaries. Although these measurements only observe the relative change in the thermal conductance, the correlation with the Seebeck measurements and the phase diagram of Bi imply that there may be a change in the thermal behavior of the material as it transitions from the Bi-I through Bi-III phases.

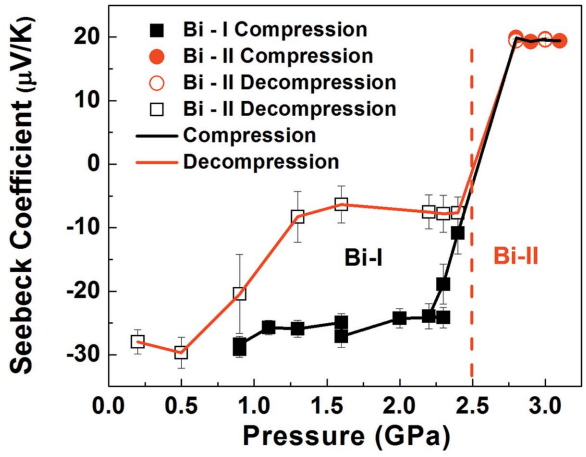

(*a*)

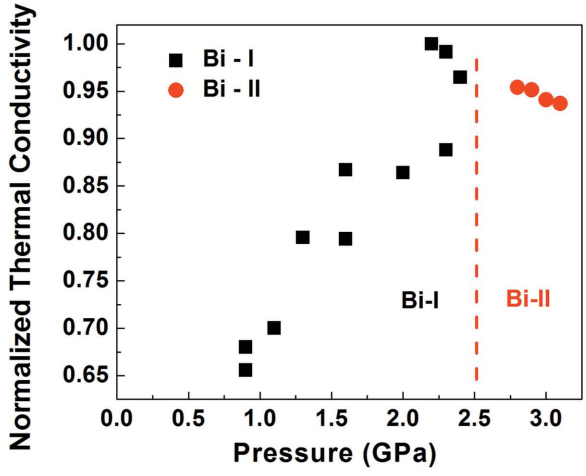

(*b*)

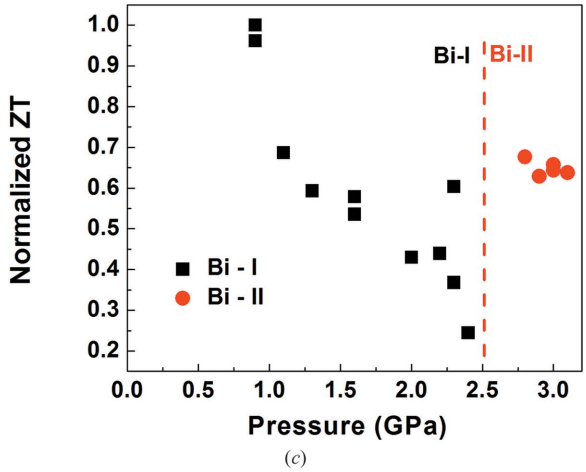

(*c*)

Figure 8
(*a*) Isothermal Seebeck coefficient measurements for compression and decompression of the bismuth sample at 325 K. The sharp variation and the change of sign of the Seebeck coefficient between 2 GPa and 2.7 GPa correspond well with the Bi-I to Bi-II phase boundary (shown as the dotted line). A similar trend is observed with decompression, but with a large hysteresis. The errors are propagated from those of voltage values. (*b*) The relative change in the thermal conductance for compression of bismuth at 325 K. The abrupt trend reversal at 2.5 GPa corresponds to the Bi-I to Bi-II transition in bismuth. (*c*) The relative change in the figure of merit (normalized by the largest value), ZT, for compression for bismuth. The discontinuity in the trend at around 2.5 GPa is consistent with those observed in the Seebeck and thermal measurements.

Fig. 8(*c*) shows a plot of the calculated dimensionless figure of merit normalized by the largest value as mentioned previously. The Seebeck coefficient and thermal conductivity were obtained in the measurements performed in this article, while the resistance values were measured and described previously using the same setup (Baker *et al.*, 2014). ZT seems to generally decrease in the Bi-I phase (below 2.5 GPa); however, at the Bi-I to Bi-II phase boundary the relative value for ZT seems to increase suddenly. This sudden increase correlates to the changes observed in the Seebeck coefficient, thermal conductivity and resistance measurements and infers that the Bi-II phase may have an increased thermoelectric efficiency as compared with the Bi-I phase at elevated pressures.

3.3. Isobaric Seebeck coefficient of PbTe

Figs. 9(*a*) and 9(*b*) display the isobaric Seebeck coefficient measurements performed on the PbTe sample at 1.0 GPa and 2.1 GPa which correspond to the pathways indicated in Fig. 3(*b*) labeled E and F, respectively. The gradual increase in the absolute value of the Seebeck coefficient agrees with the trend reported in the literature for PbTe and no phase transition is expected at these pressures and temperatures. The

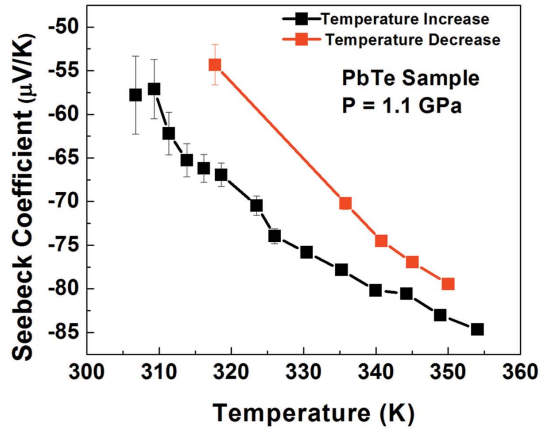

(*a*)

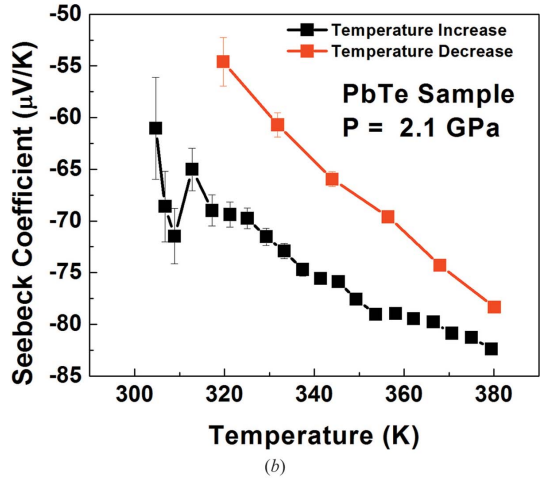

(*b*)

Figure 9
Seebeck coefficient as a function of increasing and decreasing temperature for PbTe at (*a*) 1.0 GPa and (*b*) 2.1 GPa.

hysteresis observed in the PbTe sample is similar to the hysteresis previously mentioned in the bismuth sample.

The softening of the boron epoxy gasket with increasing temperature possibly leads to a small variation in pressure or stress state of the sample as temperature is then decreased. The scatter observed in both measurements below 310 K is due to the small ΔT across the sample yielding a small voltage across the sample. This smaller voltage has a larger error and this leads to a larger scattering of the data points.

3.4. Isothermal Seebeck coefficient, resistance, thermal conductance and figure of merit of PbTe

The isothermal Seebeck coefficient measurements on PbTe compressed up to 5.5 GPa at 325 K corresponding to the path G in Fig. 3(*b*) are displayed in Fig. 10. Measurements upon decompression were not obtained because of failure of the thermocouple wires at the highest pressure (∼5.5 GPa). PbTe is known to undergo a phase transition at 6 GPa (Ovsyannikov & Shchennikov, 2007), but because of the failure of the thermocouples this transition was unobtainable in this measurement. The measurements in Fig. 10(*a*) can be compared with the measurements performed by Ovsyannikov & Shchennikov (2007) that show a similar trend for the Seebeck coefficient. The trend observed in both measurements shows a gradual decrease in the absolute value of the Seebeck coefficient from 2.0 GPa until 5.0 GPa. Ovsyannikov's measurements after 5.0 GPa begin to turn over and a gradual increase in the absolute value of the Seebeck coefficient is observed (Ovsyannikov & Shchennikov, 2007). However, our measurements do not reveal such an onset, which necessitates further investigation to confirm the isostructural thermoelectric onset. An improvement of the cell performance without breaking the wires is highly desired.

Also, the absolute value as measured by Ovsyannikov & Shchennikov (2007) at 2.5 GPa is approximately $-100\ \mu V\ K^{-1}$ with a 20% relative error reported compared with our value of $-62 \pm 1\ \mu V\ K^{-1}$. Although the values differ significantly, the error reported by Ovsyannikov, about 20%, on their Seebeck coefficient measurements is larger than the errors on our measurements, which are typically 5% or less. It should be noted that the samples studied by Ovsyannikov were single crystals and the measurements performed in this study were on polycrystalline samples, which may lead to differences in the absolute measurements of the Seebeck coefficient (Ovsyannikov & Shchennikov, 2007).

The relative measurement of the thermal conductance as the sample is compressed is shown in Fig. 10(*b*). It reveals a

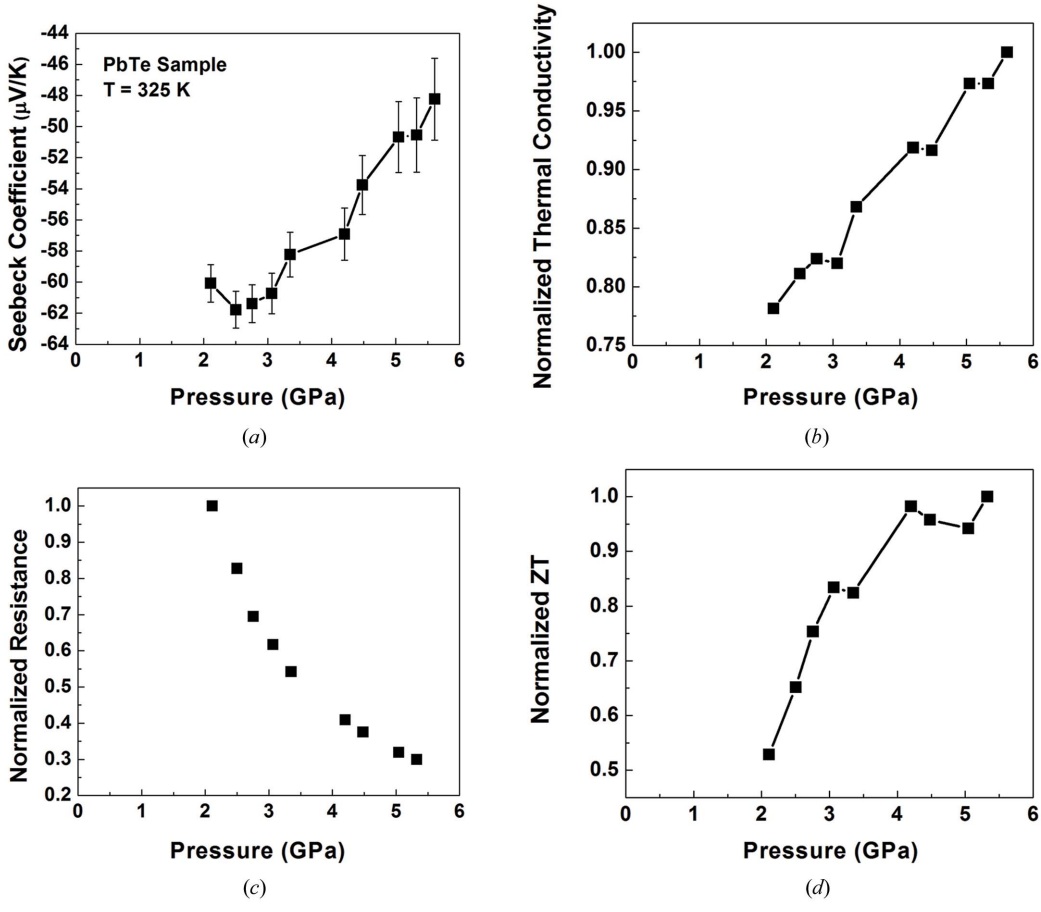

Figure 10
(*a*) Seebeck coefficient, (*b*) measurement of the relative change in the thermal conductance, (*c*) measurement of the relative change in electrical resistance carried out simultaneously with (*a*) and (*b*), and (*d*) the relative change in ZT as calculated from the values obtained for the other measurements shown.

linear increase in the conductance over the entire pressure range measured. As there is no phase transition expected in this range, this continuous linear behavior is reasonable and qualitatively agrees with the monotonous trend in the Seebeck coefficient. The resistance of the PbTe sample as measured using the Agilent multimeter, as with the other measurements, is shown in Fig. 10(*c*). The trend of decreasing resistance as the sample is compressed is in agreement with data in the literature (Ovsyannikov & Shchennikov, 2007). Combining these three measurements, the figure of merit can be calculated and is shown in Fig. 10(*d*) as the relative change in the calculated figure of merit, ZT. As shown in Fig. 10(*d*), there seems to be a fairly marked increase in the relative value of ZT as pressure is increased. This correlates well with the observed large increase in the thermoelectric efficiency as described by Ovsyannikov & Shchennikov (2007). However, our data include the effect of the thermal conductivity, at least in a qualitative fashion. Including the relative changes in the thermal conductance allows for a description of the dimensionless figure of merit ZT, which is directly correlated with the effectiveness of thermoelectric materials.

4. Conclusions

A sample cell assembly has been developed for measurement of the Seebeck coefficient and relative changes of thermal conductance and electrical resistance under high *P*–*T* conditions in the Paris-Edinburgh cell. The ability to measure all of these quantities simultaneously is unique among other techniques developed (Matityahu *et al.*, 2015; Yuan *et al.*, 2014; Li & Liebermann, 2007; Li *et al.*, 1996, 2004; Jacobsen *et al.*, 2012). The Seebeck coefficient is determined by measuring the thermoelectric voltages across the thermocouple wires located above and beneath the sample. The results show that these techniques are a valuable tool for probing electrothermal properties of thermoelectric materials across the phase boundaries. Our measurements on a Bi sample show a gradual decrease in the absolute value of the Seebeck coefficient with pressure, in agreement with a similar trend reported in the literature previously. Also, the trend observed in the Seebeck coefficient measurements performed with increasing pressure for the Bi sample across the Bi-I to Bi-II phase boundary agrees well with the reported behavior of bismuth with increasing pressure. The relative change in the thermal conductance as the sample is compressed corresponds well with the phase boundary and the observations made in the Seebeck coefficient measurements. A change in slope is observed in the relative thermal conductance measurement, which also appears in the relative change in the dimensionless figure of merit near and across the phase boundary. In addition to the measurements on bismuth, the classical thermoelectric material PbTe was studied under both isobaric and isothermal conditions. The resulting trends observed agree with the studies reported on PbTe in the literature.

Although there have been many successes with our apparatus, there are aspects that need further study as well. From our measurements, it seems that obtaining an absolute value for the Seebeck coefficient may be an issue. In addition, there is a strong need to understand the thermal properties of the cell assembly's constituent materials so as to enable modeling of the thermal flow at elevated pressures and temperatures. This would allow for an absolute value of the thermal conductivity to be obtained instead of only relative changes with pressure. Also, this would help enable an accurate determination of the thermoelectric figure of merit. Further investigations must be undertaken to refine these measurements using our apparatus.

Acknowledgements

This work was performed at HPCAT (Sector 16), Advanced Photon Source (APS), Argonne National Laboratory. HPCAT operations are supported by DOE-NNSA under Award No. DE-NA0001974 and DOE-BES under Award No. DE-FG02-99ER45775, with partial instrumentation funding by NSF. The Advanced Photon Source is a US Department of Energy (DOE) Office of Science User Facility operated for the DOE Office of Science by Argonne National Laboratory under Contract No. DE-AC02-06CH11357. Los Alamos National Laboratory (LANL) is operated by LANS, LLC, for the DOE-NNSA under Contract No. DE-AC52-06NA25396. The authors would like to thank Duygu Yazici and Brian Maple for the PbTe sample and Tony Connolly, Howard Yanxon and Vahe Mkrtchyan for aid with experiments at the beamline. The authors would like to mention appreciation for the discussions with Yoshio Kono, and the continued support of Yusheng Zhao is appreciated.

References

Badding, J. V., Meng, J. F. & Polvani, D. A. (1998). *Chem. Mater.* **10**, 2889–2894.
Baker, J., Kumar, R., Velisavljevic, N., Park, C., Kenny-Benson, C., Kono, Y., Cornelius, A. & Zhao, Y. (2014). *J. Phys. C*, **500**, 142003.
Bridgman, P. W. (1922). *Proc. Am. Acad. Arts Sci.* **57**, 75–127.
Bridgman, P. W. (1952). *Proc. Am. Acad. Arts Sci.* **81**, 165.
Bundy, F. P. (1961). *J. Appl. Phys.* **32**, 483–488.
Chandrasekhar, B. S. (1959). *J. Phys. Chem. Solids*, **11**, 268–273.
Chen, J. H., Iwasaki, H. & Kikegawa, T. (1997). *J. Phys. Chem. Solids*, **58**, 247–255.
Chung, D. Y., Hogan, T., Brazis, P., Rocci-Lane, M., Kannewurf, C., Bastea, M., Uher, C. & Kanatzidis, M. G. (2000). *Science*, **287**, 1024–1027.
DiSalvo, F. J. (1999). *Science*, **285**, 703–706.
Errandonea, D., Segura, A., Manjón, F. J., Chevy, A., Machado, E., Tobias, G., Ordejón, P. & Canadell, E. (2005). *Phys. Rev. B*, **71**, 125206.
Errandonea, D., Segura, A., Martínez-García, D. & Muñoz-San Jose, V. (2009). *Phys. Rev. B*, **79**, 125203.
Errandonea, D., Segura, A., Sánchez-Royo, J. F., Muñoz, V., Grima, P., Chevy, A. & Ulrich, C. (1997). *Phys. Rev. B*, **55**, 16217–16225.
Ferdin, B. T., Jaya, N. V., Anbukumaran, K. & Natarajan, S. (1995). *Rev. Sci. Instrum.* **66**, 5636–5637.
Jacobsen, M. K., Liu, W. & Li, B. (2012). *Rev. Sci. Instrum.* **83**, 093903.
Ke, F., Yang, J., Liu, C., Wang, Q., Li, Y., Zhang, J., Wu, L., Zhang, X., Han, Y., Wu, B., Ma, Y. & Gao, C. (2013). *J. Phys. Chem. C*, **117**, 6033–6038.
Klotz, S., Hamel, G. & Frelat, J. (2004). *High. Press. Res.* **24**, 219–223.
Kono, Y., Irifune, T., Higo, Y., Inoue, T. & Barnhoorn, A. (2010). *Phys. Earth Planet. Inter.* **183**, 196–211.

Kono, Y., Park, C., Kenney-Benson, C., Shen, G. & Wang, Y. (2014). *Phys. Earth Planet. Inter.* **228**, 269–280.
Kono, Y., Park, C., Sakamaki, T., Kenny-Benson, C., Shen, G. & Wang, Y. (2012). *Rev. Sci. Instrum.* **83**, 033905.
Li, B., Jackson, I., Gasparik, T. & Liebermann, R. C. (1996). *Phys. Earth Planet. Inter.* **98**, 79–91.
Li, B., Kung, J. & Liebermann, R. C. (2004). *Phys. Earth Planet. Inter.* **143–144**, 559–574.
Li, B. & Liebermann, R. C. (2007). *Proc. Natl Acad. Sci. USA*, **104**, 9145–9150.
Matityahu, S., Emuna, M., Yahel, E., Makov, G. & Greenberg, Y. (2015). *Rev. Sci. Instrum.* **86**, 043902.
Morard, G., Mezouar, M., Rey, N., Poloni, R., Merlen, A., Le Floch, S., Toulemonde, P., Pascarelli, S., San-Miguel, A., Sanloup, C. & Fiquet, G. (2007). *High. Press. Res.* **27**, 223–233.
Nieto-Sanz, D., Loubeyre, P., Crichton, W. & Mezouar, M. (2004). *Phys. Rev. B*, **70**, 214108.
Nishihara, Y., Fuke, K., Tange, Y. & Higo, Y. (2016). *High. Press. Res.* **36**, 121–139.
Ovsyannikov, S. V. & Shchennikov, V. V. (2004*a*). *Solid State Commun.* **132**, 333–336.
Ovsyannikov, S. V. & Shchennikov, V. V. (2004*b*). *Phys. Status Solidi B*, **241**, 3231–3234.
Ovsyannikov, S. V. & Shchennikov, V. V. (2007). *Appl. Phys. Lett.* **90**, 122103.
Ovsyannikov, S. V., Shchennikov, V. V., Todo, S. & Uwatoko, Y. (2008*a*). *High. Press. Res.* **28**, 601–606.
Ovsyannikov, S. V., Shchennikov, V. V., Todo, S. & Uwatoko, Y. (2008*b*). *J. Phys. Condens. Matter*, **20**, 172201.
Polvani, D., Meng, J., Hasegawa, M. & Badding, J. (1999). *Rev. Sci. Instrum.* **70**, 3586.
Sales, B. C. (2002). *Science*, **295**, 1248–1249.
Shchennikov, V. V., Ovsyannikov, S. V. & Bazhenov, A. V. (2008). *J. Phys. Chem. Solids*, **69**, 2315–2324.
Yamada, A., Wang, Y., Inoue, T., Yang, W., Park, C., Yu, T. & Shen, G. (2011). *Rev. Sci. Instrum.* **82**, 015103–015107.
Yuan, B., Tao, Q., Zhao, X., Cao, K., Cui, T., Wang, X. & Zhu, P. (2014). *Rev. Sci. Instrum.* **85**, 013904.